Radiative transport in the diffusion approximation: An extension for highly absorbing media and small source-detector separations

V. Venugopalan,[1,2,*] J. S. You,[1] and B. J. Tromberg[1]
[1]*Laser Microbeam and Medical Program, Beckman Laser Institute and Medical Clinic, 1002 Health Sciences Road, University of California, Irvine, Irvine, California 92612-3010*
[2]*Department of Engineering, Harvey Mudd College, Claremont, California 91711-5990*
(Received 24 February 1998)

The diffusion approximation to the Boltzmann transport equation is commonly used to analyze data obtained from biomedical optical diagnostic techniques. Unfortunately, this approximation has significant limitations to accurately predict radiative transport in turbid media, which constrains its applicability to highly scattering systems. Here we extend the diffusion approximation in both stationary and frequency-domain cases using an approach initially formulated independently by Prahl [Ph.D. thesis, University of Texas at Austin, 1988 (unpublished)] and Star [in *Dosimetry of Laser Radiation in Medicine and Biology*, edited by G. J. Müller and D. H. Sliney (SPIE, Bellingham, WA, 1989), pp. 146–154; in *Optical-Thermal Response of Laser-Irradiated Tissue*, edited by A. J. Welch and M. J. C. van Gemert (Plenum, New York, 1995), pp. 131–206]. The solution is presented in the stationary case for infinite media with a collimated source of finite size exhibiting spherical symmetry. The solution is compared to results given by standard diffusion theory as well as to measurements made in turbid phantoms with reduced single scattering albedos a' ranging from 0.248 to 0.997. Unlike the conventional diffusion approximation, the approach presented here provides accurate descriptions of optical dosimetry in both low and high scattering media. Moreover, it accurately describes the transition from the highly anisotropic light distributions present close to collimated sources to the nearly isotropic light distribution present in the far field. It is postulated that the ability to measure the transition between this near and far field behavior and predict it within a single theoretical framework may allow the separation of the single scattering anisotropy g from the reduced scattering coefficient μ_s'. The generalized formulation of diffusion theory presented here may enable the quantitative application of present optical diagnostic techniques to turbid systems which are more highly absorbing and allow these systems to be probed using smaller source-detector separations. [S1063-651X(98)13408-6]

PACS number(s): 87.90.+y, 05.60.+w, 42.62.Be

I. INTRODUCTION

The diffusion approximation for radiative transport in turbid media is used as the conceptual basis to analyze measurements made in many diagnostic biomedical laser applications. These applications, which include photon migration and fluorescence spectroscopy, have been successfully employed to determine and image tissue optical properties, quantify concentrations of physiologically relevant biomolecules, and extract accurate fluorescence and Raman spectra of turbid tissues [1–5]. Furthermore, it has been demonstrated that data of this type can form the basis for noninvasive discrimination between normal and diseased tissues [6].

Despite these successes, the standard diffusion approximation and its generalized variant, the P_1 approximation, have significant limitations [7–9]. These models provide accurate predictions for radiative transport only when the absorption coefficient μ_a is much lower than the reduced scattering coefficient μ_s' for the standard diffusion approximation or much lower than the scattering coefficient μ_s for the P_1 approximation. Further, even when the appropriate condition is satisfied, the resulting predictions are inaccurate when applied to positions proximal to the laser irradiation site. This occurs because the diffusion approximation is unable to accommodate a strong angular anisotropy in the light field such as that created in the neighborhood of a collimated light source. Also, the solution provided by the diffusion approximation in semi-infinite geometries is inaccurate proximal to interfaces where there is a refractive index mismatch. This inaccuracy arises due to issues concerning the modeling of the photon sources, the relative magnitudes of the diffuse fluence rate relative to the radiant flux, and the treatment of boundary conditions using monopole and dipole approximations [10]. All these factors result in an approximate solution to an equation that in itself represents an approximation to radiative transport theory.

Following an approach proposed independently by Prahl [11] and Star [12,13], we provide a generalized diffusion approximation to the Boltzmann transport equation for both stationary and frequency-domain cases. This generalized model explicitly includes a collimated source in the radiance approximation. It is the scattering of this collimated source that ''generates'' the diffuse light. In addition, the δ-Eddington approximation is employed to model the single scattering phase function and better accommodates media that display strong forward scattering such as tissue. We provide the solution for the stationary case in an infinite medium containing a collimated spherical source of finite size and compare it to experimental measurements made in turbid

*Author to whom correspondence should be addressed. FAX: (949) 824-8413. Electronic address: vasan@bli.uci.edu

phantoms with reduced single scattering albedo a' varying from 0.248 to 0.997. We also compare the solution to that given by the standard diffusion approximation and will demonstrate that the generalized approach shown here is accurate over a broader range of optical properties and at positions proximal to a collimated source.

II. THEORETICAL FORMULATION

A. Governing equations

Following the approach outlined by Star [13], but with the inclusion of all time-dependent terms, the following equations specify the diffuse fluence rate $\varphi_d(\mathbf{r},t)$ and the radiant flux $\mathbf{j}(\mathbf{r},t)$ within the P_1 approximation to the Boltzmann transport equation (BTE) using the δ-Eddington approximation for the scattering phase function:

$$\begin{aligned}\nabla^2\varphi_d(\mathbf{r},t)-3\mu_a\mu_{\rm tr}\varphi_d(\mathbf{r},t)&\\ -\frac{3}{v^2}\frac{\partial^2\varphi_d(\mathbf{r},t)}{\partial t^2}-\frac{3(\mu_a+\mu_{\rm tr})}{v}\frac{\partial\varphi_d(\mathbf{r},t)}{\partial t}&\\ =-3\mu_s^*\mu_{\rm tr}\,P(\mathbf{r},\hat{\mathbf{s}}_0,t)+3g^*\mu_s^*\nabla P(\mathbf{r},\hat{\mathbf{s}}_0,t)\hat{\mathbf{s}}_0&\\ -\frac{3}{v^2}\frac{\partial^2 P(\mathbf{r},\hat{\mathbf{s}}_0,t)}{\partial t^2}+\frac{3(\mu_{\rm tr}-\mu_s^*)}{v}\frac{\partial P(\mathbf{r},\hat{\mathbf{s}}_0,t)}{\partial t}&\\ -\frac{3}{v}\nabla\frac{\partial}{\partial t}[\hat{\mathbf{s}}_0P(\mathbf{r},\hat{\mathbf{s}}_0,t)],&\qquad(1)\end{aligned}$$

$$\begin{aligned}\mathbf{j}(\mathbf{r},t)=\mathcal{K}^{-1}\Big\{-\frac{1}{3}\nabla\varphi_d(\mathbf{r},t)+g^*\mu_s^*P(\mathbf{r},\hat{\mathbf{s}}_0,t)\hat{\mathbf{s}}_0&\\ -\frac{1}{v}\frac{\partial}{\partial t}[\hat{\mathbf{s}}_0P(\mathbf{r},\hat{\mathbf{s}}_0,t)]\Big\},&\qquad(2)\end{aligned}$$

where the operator $\mathcal{K}\equiv[(1/v)(\partial/\partial t)+\mu_{\rm tr}]$. In these equations, $P(\mathbf{r},\hat{\mathbf{s}}_0,t)$ is the irradiance distribution of the collimated source, $\mathbf{r}$ the position in the medium, t the time, v the speed of light in the medium, and $\hat{\mathbf{s}}_0$ the unit vector collinear with the direction of the collimated source. $\mu_{\rm tr}$ is the transport coefficient equivalent to $[\mu_a+\mu_s(1-g)]$, g being the single scattering anisotropy. μ_s^* is a reduced scattering coefficient equivalent to $\mu_s(1-f)$, where f is the fraction of light scattered directly forward in the δ-Eddington approximation to the scattering phase function. g^* is a reduced single scattering anisotropy equivalent to $g/(g+1)$. A complete derivation of the above equations and a description of the parameters is given in Appendix A. Within this formulation, the total fluence rate in the medium $\varphi(\mathbf{r},t)$ is given by the sum of the diffuse fluence rate $\varphi_d(\mathbf{r},t)$ and the collimated fluence rate $\varphi_c(\mathbf{r},t)$ defined as

$$\varphi_c(\mathbf{r},t)=\int_{4\pi}L_c(\mathbf{r},\hat{\mathbf{s}},t)d\Omega=P(\mathbf{r},\hat{\mathbf{s}}_0,t),\qquad(3)$$

where $L_c(\mathbf{r},\hat{\mathbf{s}},t)$ is the collimated radiance, $\hat{\mathbf{s}}$ the unit vector in the direction of photon travel, and Ω the solid angle.

B. Boundary conditions

For semi-infinite geometries, we must specify conditions at the top boundary, that is, the interface between the turbid media and its surroundings, as well as at infinity. At any interface where there is a refractive index mismatch, we require conservation of the diffuse radiance $L_d(\mathbf{r},\hat{\mathbf{s}},t)$. Denoting the inward surface normal at such an interface as $\hat{\mathbf{s}}_0$, this condition is expressed by

$$\begin{aligned}\int_{\hat{\mathbf{s}}\cdot\hat{\mathbf{s}}_0\geq 0}L_d(\mathbf{r},\hat{\mathbf{s}},t)(\hat{\mathbf{s}}\cdot\hat{\mathbf{s}}_0)d\hat{\mathbf{s}}&\\ =\int_{\hat{\mathbf{s}}\cdot\hat{\mathbf{s}}_0<0}L_d(\mathbf{r},\hat{\mathbf{s}},t)r_F(-\hat{\mathbf{s}}\cdot\hat{\mathbf{s}}_0)(-\hat{\mathbf{s}}\cdot\hat{\mathbf{s}}_0)d\hat{\mathbf{s}},&\qquad(4)\end{aligned}$$

where $r_F(-\hat{\mathbf{s}}\cdot\hat{\mathbf{s}}_0)$ is the Fresnel reflection coefficient for unpolarized light. Note that we conserve only the diffuse component of the radiance because the collimated component is really a source. Substituting the radiance approximation specified by the P_1 approximation [see Eq. (A15) in Appendix A] into this conservation equation and simplifying gives

$$\begin{aligned}\varphi_d(\mathbf{r},t)-Ah\nabla\varphi_d(\mathbf{r},t)\cdot\hat{\mathbf{s}}_0+\frac{3h}{2v}\frac{\partial\varphi_d(\mathbf{r},t)}{\partial t}&\\ =-3Ah\left[g^*\mu_s^*P(\mathbf{r},\hat{\mathbf{s}}_0,t)\cdot\hat{\mathbf{s}}_0-\frac{1}{v}\hat{\mathbf{s}}_0\frac{\partial P(\mathbf{r},\hat{\mathbf{s}}_0,t)}{\partial t}\right],&\qquad(5)\end{aligned}$$

where $A=(1+R_2)/(1-R_1)$, $h=2/3\mu_{\rm tr}$, $R_1=2\int_0^1 r_F(\nu_0)\nu_0 d\nu_0$, and $R_2=3\int_0^1 r_F(\nu_0)\nu_0^2 d\nu_0$. ν_0 is the cosine of the angle between the photon direction unit vector $\hat{\mathbf{s}}$ and the outward unit surface normal $-\hat{\mathbf{s}}_0$. The condition at infinity simply requires that the diffuse radiance go to zero, i.e.,

$$\varphi_d(\mathbf{r},t)(\mathbf{r}\rightarrow\infty,t)\rightarrow 0.\qquad(6)$$

III. THE CASE OF A SEMI-INFINITE SPHERICAL MEDIUM

A. Problem formulation and solution

Consider, as shown in Fig. 1, a semi-infinite medium with an inner radius of r_0 representing a collimated source of finite size that is amplitude modulated in time. In this case, the collimated irradiance $P(\mathbf{r},\hat{\mathbf{s}},t)$ takes the form

$$\begin{aligned}P(\mathbf{r},\hat{\mathbf{s}},t)=\frac{P_0\exp[-\mu_t^*(r-r_0)]}{4\pi r^2}&\\ \times\delta(1-\hat{\mathbf{s}}\cdot\hat{\mathbf{r}})\{1+M\,\exp[-i(\omega t+\epsilon)]\},&\qquad(7)\end{aligned}$$

where P_0 is the output power of the source, M the amplitude of the power modulation, ω the angular frequency, and ϵ an arbitrary phase offset. The reader should note that in a spherical geometry a ''collimated'' source is one where the photons are emitted in a direction perpendicular to the source surface as shown in Fig. 1.

To solve the governing equations, we separate the diffuse fluence rate into a time invariant or dc contribution and an oscillating or ac contribution, i.e.,

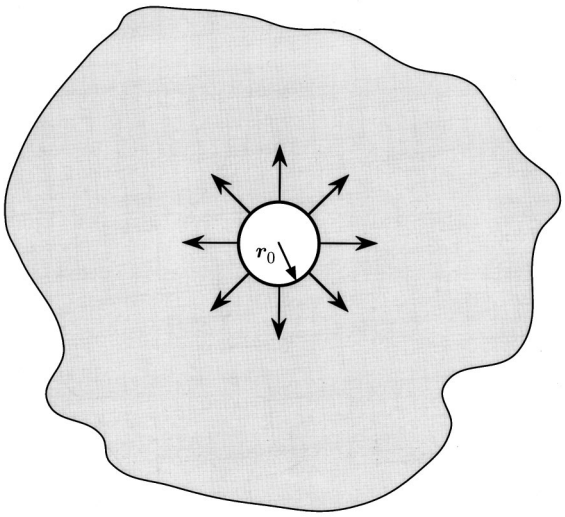

FIG. 1. Schematic of model geometry.

$$\varphi_d(\mathbf{r},t)=\varphi_d^{\mathrm{dc}}(\mathbf{r})+\varphi_d^{\mathrm{ac}}(\mathbf{r})\exp[-i(\omega t+\epsilon)]. \tag{8}$$

Substituting Eqs. (7) and (8) into Eq. (1) generates the equations

$$\nabla^2\varphi_d^{\mathrm{dc}}(\mathbf{r})-3\mu_a\mu_{\mathrm{tr}}\varphi_d^{\mathrm{dc}}(\mathbf{r}) =-3\mu_s^*(\mu_t^*+g^*\mu_a)\,\frac{P_0\exp[-\mu_t^*(r-r_0)]}{4\pi r^2}, \tag{9}$$

$$\nabla^2\varphi_d^{\mathrm{ac}}(\mathbf{r})-3\left[\mu_a\mu_{\mathrm{tr}}-\frac{\omega^2}{v^2}-\frac{i\omega(\mu_a+\mu_{\mathrm{tr}})}{v}\right]\varphi_d^{\mathrm{ac}}(\mathbf{r}) =-3\left[\mu_s^*(\mu_t^*+g^*\mu_a)-\frac{\omega^2}{v^2}+\frac{i\omega(\mu_{\mathrm{tr}}+\mu_a)}{v}\right] \times\frac{P_0M\,\exp[-\mu_t^*(r-r_0)]}{4\pi r^2}, \tag{10}$$

where μ_t^* is the effective interaction coefficient equivalent to $\mu_a+\mu_s^*$. In an analogous fashion we generate two sets of boundary conditions. For the interface between the source surface and the turbid media, i.e., at $r=r_0$, we substitute Eq. (8) into Eq. (5), which yields

$$\varphi_d^{\mathrm{dc}}(\mathbf{r})-Ah\nabla\varphi_d^{\mathrm{dc}}(\mathbf{r})\cdot\hat{\mathbf{r}}=\frac{-3Ahg^*\mu_s^*P_0}{4\pi r_0^2}, \tag{11}$$

$$\varphi_d^{\mathrm{ac}}(\mathbf{r})-\left(\frac{2Ahv}{2v-3i\omega h}\right)\nabla\varphi_d^{\mathrm{ac}}(\mathbf{r})\cdot\hat{\mathbf{r}} =\frac{-6Ahv}{2v-3i\omega h}\left(g^*\mu_s^*+\frac{i\omega}{v}\right)\frac{P_0M}{4\pi r_0^2}. \tag{12}$$

For $r\to\infty$ we substitute Eq. (8) into Eq. (6), which gives

$$\varphi_d^{\mathrm{dc}}(\mathbf{r}),\varphi_d^{\mathrm{ac}}(\mathbf{r})\to 0 \tag{13}$$

In this study we consider only the solution of the dc component for the diffuse fluence rate. The method of solution is detailed in Appendix B. The solution to Eq. (9) subject to the boundary conditions specified by Eqs. (11) and (13) is

$$\varphi_d^{\mathrm{dc}}(\mathbf{r})=\frac{3\mu_s^*(\mu_t^*+g^*\mu_a)P_0\exp(\mu_t^*r_0)}{8\pi\mu_{\mathrm{eff}}\,r} \times\left\{\left[E_1(\mu_t^*r_0-\mu_{\mathrm{eff}}\,r_0)-E_1(\mu_t^*r_0+\mu_{\mathrm{eff}}\,r_0) -\frac{2g^*\sinh(\mu_{\mathrm{eff}}\,r_0)}{r_0(\mu_t^*+g^*\mu_a)\exp(\mu_t^*r_0)} -E_1(\mu_t^*r-\mu_{\mathrm{eff}}r)\right]\exp(-\mu_{\mathrm{eff}}\,r) +E_1(\mu_t^*r+\mu_{\mathrm{eff}}\,r)\exp(\mu_{\mathrm{eff}}\,r)\right\}, \tag{14}$$

where μ_{eff} is the effective attenuation coefficient equivalent to $(3\mu_a\mu_{\mathrm{tr}})^{1/2}$ and $E_1(z)$ the exponential integral defined as $\int_z^\infty[\exp(-t)/t]dt$. Thus the total fluence rate is given by $\varphi_d^{\mathrm{dc}}(\mathbf{r})+\varphi_c^{\mathrm{dc}}(\mathbf{r})$, where $\varphi_d^{\mathrm{dc}}(\mathbf{r})$ is given by Eq. (14) and the collimated fluence rate is given by

$$\varphi_c^{\mathrm{dc}}(\mathbf{r})=P^{\mathrm{dc}}(\mathbf{r},\hat{\mathbf{s}}_0,t)=\frac{P_0\exp[-\mu_t^*(r-r_0)]}{4\pi r^2}. \tag{15}$$

At this point, the radiant flux $\mathbf{j}^{\mathrm{dc}}(\mathbf{r})$ can also be determined. The expression for $\mathbf{j}^{\mathrm{dc}}(\mathbf{r})$ is given by substituting Eq. (8) into Eq. (2):

$$\mathbf{j}^{\mathrm{dc}}(\mathbf{r})=\frac{1}{3\mu_{\mathrm{tr}}}\left[\nabla\varphi_d^{\mathrm{dc}}(\mathbf{r})+3g^*\mu_s^*P^{\mathrm{dc}}(\mathbf{r},\hat{\mathbf{s}}_0,t)\hat{\mathbf{s}}_0\right]. \tag{16}$$

Substituting Eqs. (14) and (15) into Eq. (16) yields

$$\mathbf{j}^{\mathrm{dc}}(\mathbf{r})=\frac{1}{3\mu_{\mathrm{tr}}}\left\{FG\left(\frac{\mu_{\mathrm{eff}}}{r}+\frac{1}{r^2}\right)\exp(-\mu_{\mathrm{eff}}\,r) -FH\left(\frac{\mu_{\mathrm{eff}}}{r}-\frac{1}{r^2}\right)\exp(\mu_{\mathrm{eff}}\,r) +3g\mu_s^*P_0\,\frac{\exp[-\mu_t^*(r-r_0)]}{4\pi r^2}\right\}, \tag{17}$$

where

$$F=\frac{3\mu_s^*(\mu_t^*+g^*\mu_a)P_0\exp(\mu_t^*r_0)}{8\pi\mu_{\mathrm{eff}}}, \tag{18}$$

$$G=\left[E_1(\mu_t^*r_0-\mu_{\mathrm{eff}}\,r_0)-E_1(\mu_t^*r_0+\mu_{\mathrm{eff}}\,r_0) -\frac{2g^*\sinh(\mu_{\mathrm{eff}}\,r_0)}{r_0(\mu_t^*+g^*\mu_a)\exp(\mu_t^*r_0)}-E_1(\mu_t^*r-\mu_{\mathrm{eff}}\,r)\right], \tag{19}$$

$$H=E_1(\mu_t^*r+\mu_{\mathrm{eff}}\,r). \tag{20}$$

TABLE I. Intralipid volume fractions and NiSPC concentrations used for the five turbid phantoms in which measurements were made. The optical properties of these phantoms are also listed for the wavelength tested $\lambda = 674$ nm. All phantoms had a single scattering anisotropy $g = 0.71$.

Sample No.	Intralipid (%)	NiSPC (μg/ml)	μ_a (mm^{-1})	μ_s' (mm^{-1})	μ_s'/μ_a	a'	a^*	$l^\star$ (mm)
1	0.100	0.00	4.11×10^{-4}	0.12	290	0.9966	0.9980	8.31
2	0.100	1.20	8.57×10^{-3}	0.12	14	0.9333	0.9599	7.78
3	0.100	5.72	3.93×10^{-2}	0.12	3.1	0.7534	0.8391	6.28
4	0.050	8.41	5.76×10^{-2}	0.06	1.0	0.5102	0.6403	8.50
5	0.025	13.30	9.09×10^{-2}	0.03	0.33	0.2482	0.3607	8.28

B. Limiting cases

Unique features of the solution for the diffuse fluence rate can be better seen by examining certain limiting cases. To treat an infinite medium with a true point source, we consider Eq. (14) in the limit $r_0 \to 0$, where it reduces to

$$\varphi_d^{\mathrm{dc}}(\mathbf{r}) = \frac{3\mu_s^*(\mu_t^* + g^*\mu_a)P_0}{8\pi\mu_{\mathrm{eff}}\, r} \times \left\{ \exp(\mu_{\mathrm{eff}}\, r) E_1(\mu_t^* r + \mu_{\mathrm{eff}}\, r) + \exp(-\mu_{\mathrm{eff}}\, r) \times \left[\ln\left(\frac{\mu_t^* + \mu_{\mathrm{eff}}}{\mu_t^* - \mu_{\mathrm{eff}}} \right) - \frac{2g^*\mu_{\mathrm{eff}}}{\mu_t^* + g^*\mu_a} - E_1(\mu_t^* r - \mu_{\mathrm{eff}}\, r) \right] \right\}. \quad (21)$$

We compare Eq. (21) to the solution for a point source in the conventional diffusion approximation where the fluence rate and radiant flux are given by the expressions [14]

$$\varphi^{\mathrm{dc}}(\mathbf{r}) = 3\mu_{\mathrm{tr}} \frac{P_0 \exp(-\mu_{\mathrm{eff}}\, r)}{4\pi r}, \quad (22)$$

$$\mathbf{j}^{\mathrm{dc}}(\mathbf{r}) = \frac{P_0 \exp(-\mu_{\mathrm{eff}}\, r)}{4\pi} \left(\frac{\mu_{\mathrm{eff}}}{r} + \frac{1}{r^2} \right). \quad (23)$$

We expect that when scattering is dominant, Eq. (21) should reduce to Eq. (22) in the far field. To verify this, we consider Eq. (21) in the limit where $\mu_t^* \gg \mu_{\mathrm{eff}}$ and $r \to \infty$. In this case, the contribution of collimated light is negligible and the total fluence rate is dominated by the diffuse contribution. For large z, $E_1(z) \sim \exp(-z)/z$. Thus both terms involving the exponential integral go to zero much faster than the natural log and constant terms. Further, since $\mu_t^* \gg \mu_{\mathrm{eff}}$, the natural log term is accurately approximated by the first term in the power series

$$\ln\frac{z+1}{z-1} = 2\left(\frac{1}{z} + \frac{1}{3z^2} + \cdots \right) \quad \text{for } |z| > 1, \quad (24)$$

where $z = \mu_t^*/\mu_{\mathrm{eff}}$. Making use of the power series expansion, the total fluence rate reduces to

$$\varphi^{\mathrm{dc}}(\mathbf{r}) \sim \frac{3\mu_s^*(\mu_t^* + g^*\mu_a)P_0}{8\pi\mu_{\mathrm{eff}}\, r} \times \left(\frac{2\mu_{\mathrm{eff}}}{\mu_t^*} - \frac{2g^*\mu_{\mathrm{eff}}}{\mu_t^* + g^*\mu_a} \right) \exp(-\mu_{\mathrm{eff}}\, r) = 3\mu_{\mathrm{tr}} \frac{P_0 \exp(-\mu_{\mathrm{eff}}\, r)}{4\pi r}, \quad (25)$$

which is identical to Eq. (22). Thus the generalized model agrees with standard diffusion theory in the far field for the case of dominant scattering.

Now consider the far-field behavior of Eq. (21) in the limit of high absorption, i.e., $\mu_t^* \ll \mu_{\mathrm{eff}}$. This occurs when $\mu_s^* \to 0$ and results in $\varphi_d^{\mathrm{dc}}(\mathbf{r}) \to 0$. Thus, when absorption is dominant the total fluence rate is governed solely by the collimated contribution, i.e.,

$$\varphi^{\mathrm{dc}}(\mathbf{r}) = \varphi_c^{\mathrm{dc}}(\mathbf{r}) = \left(\frac{P_0}{4\pi r^2} \right) \exp(-\mu_a r). \quad (26)$$

So, unlike the standard diffusion approximation, the generalized model correctly recovers Beer's law in the limit of no scattering.

IV. EXPERIMENT MATERIALS AND METHODS

To test the generalized model described above we performed measurements in a cylindrical Plexiglas container 18 cm in diameter and 25 cm tall filled with 6 l of turbid solution consisting of intralipid, an absorber [nickel tetrasulfonated phthalocyanine (NiSPC)], and deionized water. Table I gives the intralipid volume fraction and NiSPC concentration used for each of the five solutions tested and their optical properties at the wavelength used for the measurements, $\lambda = 674$ nm. The scattering properties of each phantom were determined using the published values for intralipid [15]. The absorption coefficient of each phantom was determined using published absorption spectra of water [16] and the measurement of NiSPC absorption when solubilized in deionized water. The latter was done using a spectrophotometer (Model DU-7, Beckman Instruments Inc., Irvine, CA) and yielded a value of $(6.8 \pm 0.1)\times10^{-3}$ mm^{-1} for a concentration of 1 μg/ml at $\lambda = 674$ nm.

A general schematic of the experiment setup is given in Fig. 2. Measurements were conducted using a 674-nm laser diode (Model 7421, SDL Inc., San Jose, CA) whose output

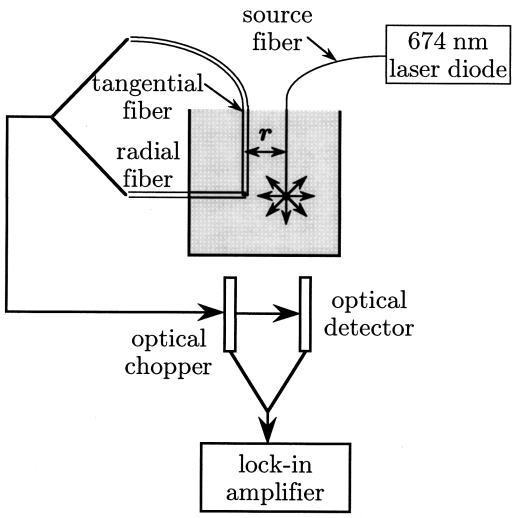

FIG. 2. Experiment setup for measurement of light transport within turbid phantoms.

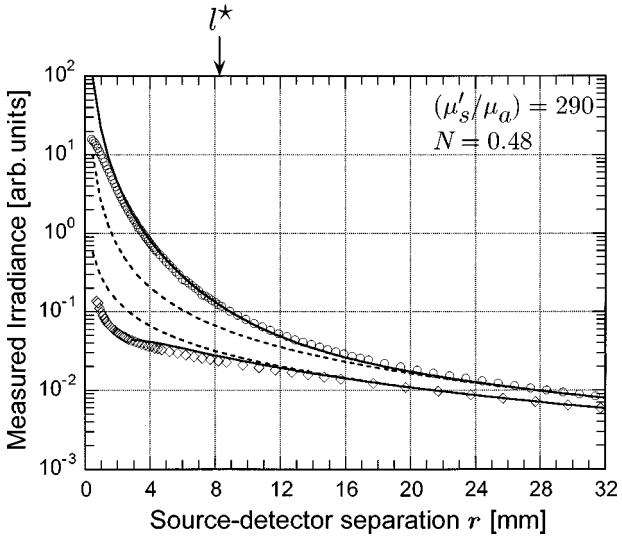

FIG. 3. Irradiance vs radial position as measured within phantom No. 1 with $(\mu_s'/\mu_a)=290$ and $l^\star=8.31$ mm. Measurements using radial (○) and tangential (◇) detection are shown and employ an optical fiber with $N=0.48$. Predictions given by the generalized diffusion model are shown by the solid curves while those given by standard diffusion theory are shown by the dashed curves.

was delivered via a 400-μm fiber coupled to an 800-μm-diam spherical diffuser (Rare Earth Medical, Yarmouth, MA). For detection, a flat-cut optical fiber was oriented either radially or tangentially to the diffuser. The transport of light within the phantom was measured at a number of distances ranging from placing the diffuser and the detection fiber in virtual contact to a source-detector separation of up to approximately 50 mm. To further investigate the angular distribution of radiation within the phantom, three different detection fibers were used at each orientation: (a) a 550-μm-core-diam silica multimode fiber with a numerical aperture $N=0.22$, (b) a 600-μm-core-diam silica multimode fiber with $N=0.37$, and (c) a 600-μm-core-diam hard clad multimode fiber with $N=0.48$. The light collected by the detection fiber was modulated by means of an optical chopper (SR 540, Stanford Research Systems, Sunnyvale, CA) and directed to an optical meter (1835-C, Newport Corporation, Irvine, CA). The electronic output from the chopper controller and optical meter were directed to a lock-in amplifier (SR 830, Stanford Research Systems, Sunnyvale, CA), which gave a reading of the collected laser diode power.

These measurements are compared to predictions made by the models described above. The measurements do not give the fluence rate in the medium directly and thus further calculations are necessary to allow a direct comparison of the model predictions with the measurements. Specifically, when the optical fiber is oriented radially or tangentially relative to the spherical source, the measured irradiances I_r and I_t are functions of the source-detector separation r and the numerical aperture N of the collection fiber. Defining $\theta \equiv[\sin^{-1}(N)/n]$, n being the refractive index of the phantom, the measured irradiances are given by the expressions

$$I_r(r,\theta)=\varphi_c^{\mathrm{dc}}(r)+\tfrac{1}{4}[\sin^2\theta\varphi_d^{\mathrm{dc}}(r)+2(1-\cos^3\theta)\mathbf{j}^{\mathrm{dc}}(r)], \tag{27}$$

$$I_t(r,\theta)=\frac{\sin^2\theta}{4}\,\varphi_d^{\mathrm{dc}}(r). \tag{28}$$

The derivation of Eqs. (27) and (28) is given in Appendix C.

The measurements were conducted such that an absolute value of the irradiance was not determined. Thus, after acquisition, the data were scaled to the predictions given by the models. In the cases presented below, the predictions given by the models approach each other at large source-detector separations. The data were scaled to the model predictions in this region and thus the accuracy of the models relative to the data is established in an absolute sense.

V. RESULTS AND DISCUSSION

Figure 3 presents the measured variation of irradiance with radial distance from the center of the spherical diffuser for both radial and tangential orientations using a detection fiber with $N=0.48$. These measurements were made in phantom 1, where optical scattering dominated absorption such that $\mu_s'/\mu_a=290$. This ratio of scattering to absorption satisfies the requirements for the validity of the standard diffusion approximation [17]. The figure also displays the irradiance predicted by both the standard diffusion approximation and the generalized model presented here. To calculate the measured irradiance in the generalized formalism, Eqs. (14), (15), and (17) are substituted in Eqs. (27) and (28), while for the standard diffusion approximation $\varphi_c^{\mathrm{dc}}(\mathbf{r})=0$ and Eqs. (22) and (23) are substituted in Eqs. (27) and (28).

There are several notable features in this figure. First, even in the far field (i.e., at large r) the measured irradiance for radial and tangential detection are noticeably different. This demonstrates that the magnitude of the radiant flux is significant and should not be neglected. Second, at these

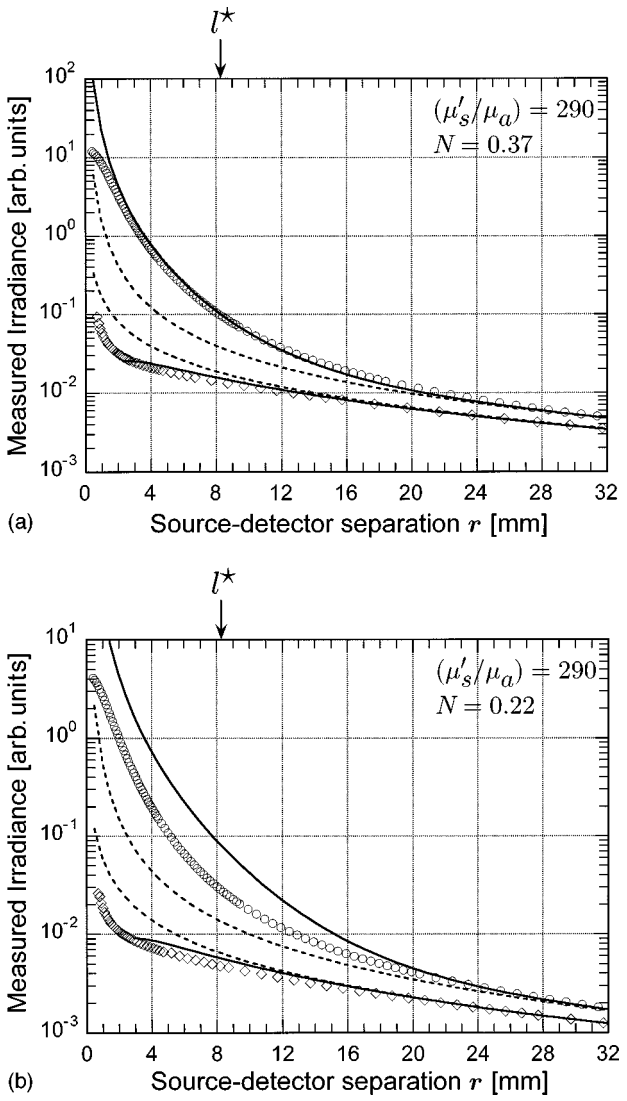

FIG. 4. Irradiance vs radial position as measured within phantom No. 1 with $(\mu_s'/\mu_a)=290$ and $l^\star=8.31$ mm. Measurements using radial (○) and tangential (◇) detection are shown and employ an optical fiber with (a) $N=0.37$ or (b) $N=0.22$. Predictions given by the generalized diffusion model are shown by the solid curves while those given by standard diffusion theory are shown by the dashed curves.

large distances the data (symbols) and the predictions given by both standard diffusion theory (dashed curves) and the generalized diffusion model presented here (solid curves) are congruent. Third, the predictions given by standard diffusion theory and the generalized model begin to diverge at $r \lesssim 3l^\star$ for radial detection and at $r \lesssim 2l^\star$ for tangential detection, where $l^\star$ is the transport mean free path and is defined by $l^\star \equiv \mu_{\rm tr}^{-1}$. Fourth, once the predictions given by the two models diverge, the generalized model provides the better prediction. Finally, at $r \lesssim l^\star/5$ for radial detection and $\lesssim l^\star/3$ for tangential detection, the prediction given by the generalized diffusion model and the data begin to disagree.

Figures 4(a) and 4(b) present results in the same phantom but for cases where the numerical aperture of the detection fiber is 0.37 and 0.22, respectively. The basic features of Fig. 3 are retained in Fig. 4(a). The only notable difference is that the ratio of the irradiance detected via radial vs tangential detection is larger. This is because for radial detection there is a significant contribution from light that is strongly forward directed, as is evident through the collimated and radiant flux terms in Eq. (27), while for tangential detection the collected light is essentially isotropic. Thus a smaller numerical aperture will reduce the tangential signal roughly in direct proportion to the reduction in solid angle collected by the fiber. In contrast, the radial signal will not be reduced as greatly since the collimated fluence rate and the radiant flux contributions are weighted along the fiber axis and not as effectively rejected through a reduction in numerical aperture. In Fig. 4(b) we see that for a detection fiber with numerical aperture of 0.22 the generalized model significantly overestimates the measured irradiance for radial detection but still gives adequate predictions for tangential detection. The failure of the generalized model at this small numerical aperture results from the inaccuracy of the δ-Eddington phase function approximation that tends to overestimate the light scattered directly into the forward peak for g values deviating significantly from unity [18]. This inaccuracy is particularly evident here since scattering is so dominant over absorption. However, note that the prediction given by the generalized model is no worse than that given by standard diffusion theory. Further, in the far field the data approach the prediction given by the generalized model more rapidly than that given by standard diffusion theory.

The performance of the generalized model continues to be impressive even for phantoms with stronger absorption, while the performance of standard diffusion theory degrades. Figures 5(a)–5(c) and 6(a)–6(c) present the measured irradiance and corresponding model predictions for both radial and tangential detection with fibers having numerical apertures of 0.48, 0.37, and 0.22 in phantoms 2 and 4, respectively. These phantoms have a ratio of reduced scattering to absorption $\mu_s'/\mu_a=14$ and 1.0, respectively. There are several notable changes in the light field that occur with the reduction of μ_s'/μ_a.

First, since the probability of absorption relative to scattering is greater in these phantoms, photons on average undergo fewer scattering events before they are absorbed. This results in an angular distribution of light that remains forward directed even at large depths within the medium. This is manifest by a large ratio of the measured irradiance using radial vs tangential detection in the far field [see, e.g., Fig. 6(c)]. This effect is well predicted by the generalized model, which is congruent to the data in the far field. Predictions made by standard diffusion theory do not fare as well and consistently underestimate the measured irradiance for radial detection. Further, in the case of dominant absorption, standard diffusion theory predicts the fluence rate to decay $\sim \exp(-\sqrt{3}\mu_a)$ [see Eq. (22)], which violates Beer's law. The performance of standard diffusion theory to predict the irradiance measured using tangential detection is notably better. However, this prediction also degrades with increasing absorption.

Second, the accuracy of the generalized model in the near field appears to degrade slightly for tangential detection with increasing absorption. Specifically, for phantom 4 the data and model fits begin to disagree noticeably for $r \lesssim 2l^\star/3$, while the accuracy in the radial configuration is maintained. Although this may be a true deficiency in the model, we

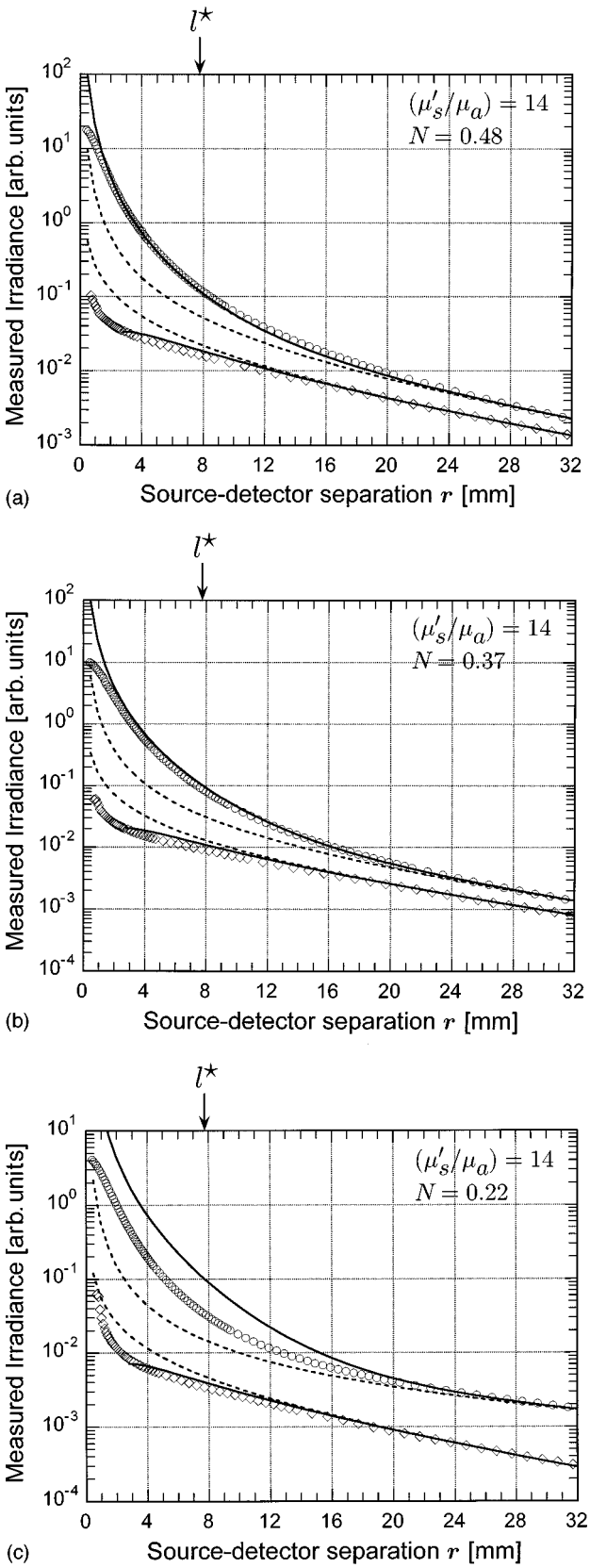

FIG. 5. Irradiance vs radial position as measured within phantom No. 2 with $(\mu_s'/\mu_a) = 14$ and $l^\star = 7.78$ mm. Measurements using radial (○) and tangential (◇) detection are shown and employ an optical fiber with (a) $N = 0.48$, (b) $N = 0.37$, or (c) $N = 0.22$. Predictions given by the generalized diffusion model are shown by the solid curves while those given by standard diffusion theory are shown by the dashed curves.

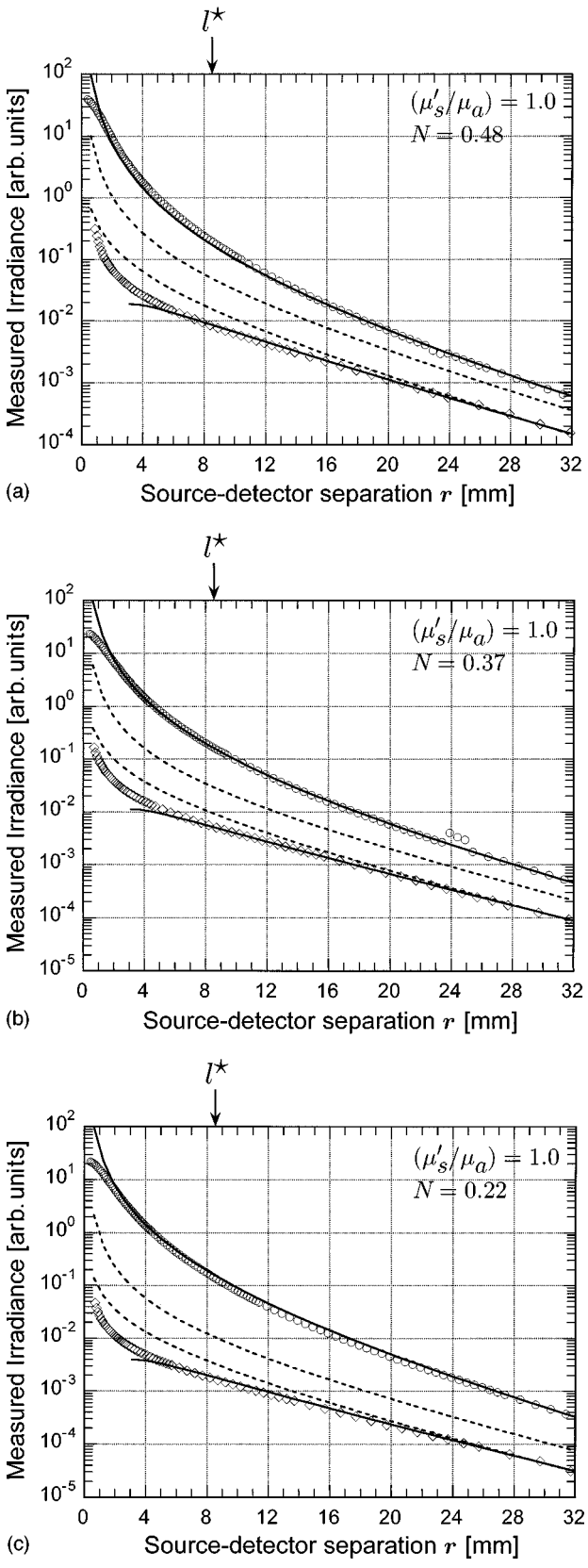

FIG. 6. Irradiance vs radial position as measured within phantom No. 4 with $(\mu_s'/\mu_a) = 1.0$ and $l^\star = 8.50$ mm. Measurements using radial (○) and tangential (◇) detection are shown and employ an optical fiber with (a) $N = 0.48$, (b) $N = 0.37$, or (c) $N = 0.22$. Predictions given by the generalized diffusion model are shown by the solid curves while those given by standard diffusion theory are shown by the dashed curves.

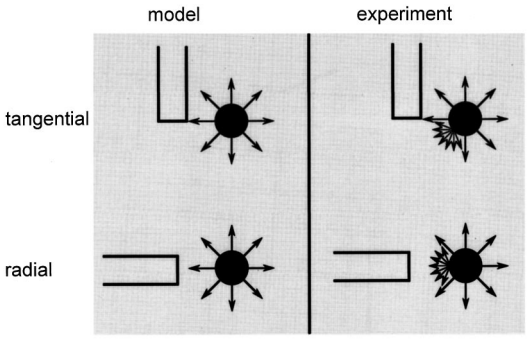

FIG. 7. Illustration of the difference between the modeling of the spherical photon source and its behavior in experiment. In experiment, the source is not collimated but emits diffusely from the surface. In tangential detection, light emitted from the source at a location where the surface normal is not parallel with the fiber face may enter the fiber as shown. For radial detection, all light emitted from the source at the location directly opposite the fiber will not be captured due to the angular spread in the emission as shown. Neither of these effects is accounted for in the optical model. See text for further details.

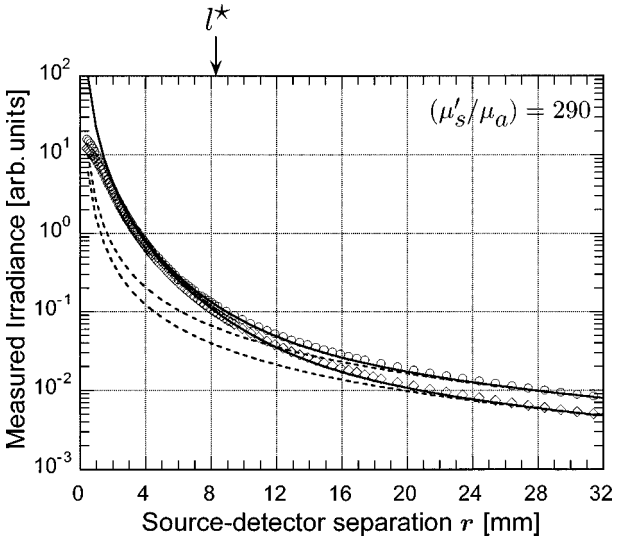

FIG. 8. Irradiance vs radial position as measured within phantom No. 1 with (μ_s'/μ_a) and $l^* = 8.31$ mm. Measurements using radial detection are shown and employ optical fiber with $N = 0.48$ (○) and $N = 0.37$ (◇). Predictions given by the generalized diffusion model are shown by the solid curves while those given by standard diffusion theory are shown by the dashed curves.

suspect that it may be due to an inability of the experimental apparatus to achieve certain conditions assumed by the optical model. Specifically, the model treats the light source as being spherically collimated, that is, all photons supplied by the source are assumed to be emitted normal to the surface of the spherical diffuser. This is not achieved by the spherical diffuser that we employ. Rather, each point on the surface of the spherical diffusing tip likely emits light with a significant angular spread. The difference between the model and experimental conditions is shown graphically in Fig. 7.

For tangential detection, this difference permits some minimally scattered or even unscattered photons to enter the detection fiber and results in a measured irradiance higher than that predicted by theory. Further, as scattering decreases, we expect the inaccuracy to be seen at larger source-detector separations. This is because if a photon is traveling on a path that would be collected by the fiber, a reduction in scattering reduces the probability that the photon would be scattered off this path. Both these characteristics are seen in Figs. 5(a)–5(c) and 6(a)–6(c). For radial detection, the inaccuracy results in a measured irradiance lower than that predicted by theory. This is because light not emitted at an angle normal to the spherical diffuser has a reduced probability of being captured by the optical fiber. In this case, the inaccuracy should be insensitive to the albedo of the solution as optical scattering should not bias the probability that light emitted at an angle oblique to the diffuser surface will be detected by the fiber.

Finally, an important observation can be made when comparing measurements using radial detection with two different numerical apertures. To illustrate this we display in Fig. 8 the data for phantom 1 using fibers with numerical apertures of 0.48 and 0.37. In the near field the data and the prediction given by the generalized model agree and both are insensitive to the difference in numerical aperture. This is because in the near field, virtually all the light is collimated and captured equally by both optical fibers. However, as r increases, an increasing number of photons are scattered out of the forward peak and the irradiance measured by a smaller numerical aperture fiber decays faster with r than for a large numerical aperture fiber. Finally, in the far field, the angular distribution of the radiance is nearly isotropic and predictions given by both the generalized and standard diffusion models are accurate. Conceptually, measurement of the irradiance decay in the near and far fields can determine values for μ_t^* and μ_{eff}, respectively. These two values can be algebraically manipulated to give μ_a and μ_s'. What is important, however, is the spatial location of the transition between near- and far-field behavior. We can effectively sample the evolution of the angular distribution of light as it travels away from the source by making measurements using two fibers of different numerical aperture at a number of radial locations within this transition region. Thus, for a fixed value of μ_a and μ_s', the location of this transition region is not fixed but is dependent on the single scattering anisotropy g. This is because for lower values of g fewer scattering events are required on average to scatter photons out of the forward peak.

Figure 9 demonstrates this by displaying the ratio of the measured irradiance using radial detection with a 0.37 numerical aperture fiber vs a 0.48 numerical aperture fiber as predicted using the generalized diffusion model. The irradiance ratio is given for fixed values of μ_a and μ_s', but with values of g ranging from 0.7 to 0.95. The values of μ_a and μ_s' were chosen to be identical to that of phantom 1. These curves clearly show the near- and far-field behavior; in the near field the irradiance ratio is near unity, while in the far field the ratio depends solely on the numerical apertures employed and the values for μ_a and μ_s' of the medium. However, while the values of μ_a and μ_s' are held fixed, increasing values of g shift the transition region between the near- and far-field behavior to smaller source-detector separations. This observation may provide the conceptual basis for determining the single scattering anisotropy of a turbid medium through multiple distance measurements using detec-

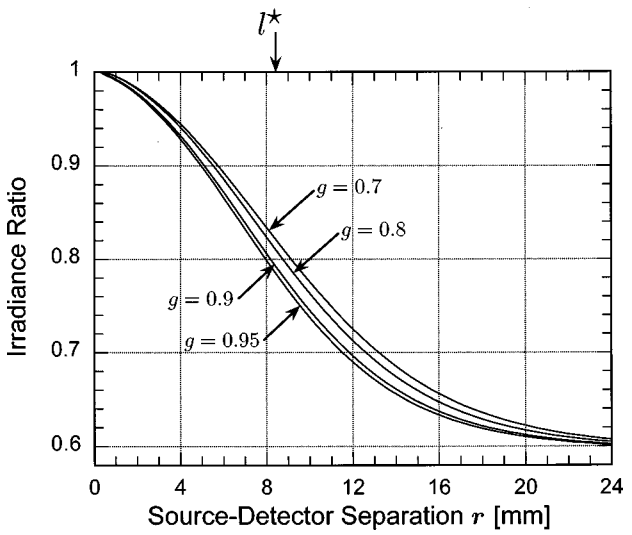

FIG. 9. The irradiance ratio detected in radial orientation using an optical fiber with $N=0.37$ vs $N=0.48$ is plotted vs radial position. The values used for μ_a and μ_s' are fixed and equal to those of phantom No. 1 but curves are shown for values of g over the range 0.7–0.95 as indicated.

tion fibers with different numerical apertures.

While these curves have been generated solely from the generalized model, we are confident that they are accurate for two reasons. First, Figs. 3 and 4(a) demonstrate that for phantom 1, where the single scattering anisotropy $g=0.71$, the prediction of the generalized model for detection using fibers with numerical aperture of 0.48 and 0.37 is excellent. Thus we have full confidence in the model results for $g=0.7$. Second, the remaining curves are generated by changing the value of g while keeping a' fixed. Thus the only potential difficulty for these other curves is the fidelity of the δ-Eddington phase function. Fortunately, the accuracy of the δ-Eddington phase function increases for increasing g [18]. Thus, for the higher g values, the model results should be no worse than those given for $g=0.7$, which we know to be accurate through our experimental study.

The benefits that this generalized diffusion model offers for time-independent (dc) measurements will likely transfer over to cases where the source is pulsed or intensity modulated. The inability of standard diffusion theory to accurately predict the phase and dc amplitude of photon density waves at positions proximal to a source has already been documented by Fantini, Franceschini, and Gratton [19]. These investigators have also shown that an effective photon source term can be constructed and used within standard diffusion theory to generate predictions that match experiment. However, these source terms were empirically derived and not developed using first principles. In contrast, the generalized diffusion model presented here is derived from the BTE and provides accurate predictions of the dc irradiance at positions proximal to the source. It thus seems reasonable to expect that once the governing equations are solved in the frequency domain [i.e., Eqs. (10), (12), and (13)], the prediction of the propagation characteristics of photon density waves close to photon sources and in strongly absorbing media should be possible as well.

VI. SUMMARY AND CONCLUSIONS

In this paper we have presented the governing equations for a generalized diffusion model in steady-state and frequency-domain cases for optical transport in turbid media based on initial work by Prahl [11] and Star [12,13]. The principal advantages this approach offers over standard diffusion theory are that it provides accurate predictions of the light distribution within turbid media at positions proximal to collimated sources and over a full range of single scattering albedo. These improvements are achieved by deviating from the standard diffusion theory approach in two ways. First, the radiance is separated into collimated and diffuse components where the optical scattering of the collimated light provides the source of diffuse light. Second, the δ-Eddington approximation is employed for the single scattering phase function, which is more accurate than the conventional Eddington approximation in modeling optical transport in media with large anisotropy.

The generalized diffusion model was applied to measurements made using a finite spherical source immersed in ''infinite'' turbid phantoms with reduced single scattering albedos ranging from 0.248 to 0.997. In all cases, predictions made by the generalized diffusion model outperformed those given by standard optical diffusion theory. Moreover, unlike standard optical diffusion theory, the generalized model has the capacity to accurately predict the transition region between the highly forward-directed light distribution proximal to the source and the nearly isotropic light distribution present in the far field. We have demonstrated that the spatial location of this transition zone is sensitive to the single scattering anisotropy g even when μ_a and μ_s' are held constant. This indicates that it may be possible to separate g from μ_s' through an appropriate combination of measurement and theory.

The use of this generalized diffusion theory shows promise to expand the situations in which spectroscopic measurements can be used to quantify optical properties of turbid media. Specifically, the model will likely permit the probing of turbid media using small source detector separations and allow the measurement of media with high absorption. For biomedical applications, this may allow the development of site-specific tissue probes and the utilization of shorter wavelengths to quantify tissue optical properties as well as concentrations of physiologically important analytes that display negligible optical absorption in the red and near infrared regions of the optical spectrum.

ACKNOWLEDGMENTS

This work was made possible, in part, by the Laser Microbeam and Medical Program at the University of California, Irvine. This facility is supported by the National Institutes of Health under Grant No. RR-01192. Support was also provided by the Department of Energy under Grant No. DE-FG03-91ER61227, and the NIH Institute of General Medical Sciences under Grant No. GM-50958. V.V. acknowledges support from the Whitaker Foundation. We thank Joshua Fishkin and Scott Prahl for many helpful discussions.

APPENDIX A: DERIVATION OF GENERALIZED DIFFUSION THEORY FROM THE BOLTZMANN TRANSPORT EQUATION

Here we derive the governing equations of the generalized diffusion model as given by Eqs. (1) and (2) above. We begin with the Boltzmann transport equation, which describes linear transport of photons traveling in a turbid media,

$$\frac{1}{v}\frac{\partial L(\mathbf{r},\hat{\mathbf{s}},t)}{\partial t}+\hat{\mathbf{s}}\cdot\boldsymbol{\nabla}L(\mathbf{r},\hat{\mathbf{s}},t) = -\mu_t L(\mathbf{r},\hat{\mathbf{s}},t)+\mu_s\int_{4\pi}L(\mathbf{r},\hat{\mathbf{s}}',t)p(\hat{\mathbf{s}},\hat{\mathbf{s}}')d\Omega + S(\mathbf{r},\hat{\mathbf{s}},t), \tag{A1}$$

where L is the radiance and S the volumetric radiance provided by a source. v, μ_s, and μ_t are the speed of photons in the medium, the scattering coefficient, and the interaction coefficient, i.e., $=\mu_a+\mu_s$, respectively. $\mathbf{r}$, $\hat{\mathbf{s}}$, t, and Ω are the position vector, unit direction vector, time, and solid angle, respectively. $p(\hat{\mathbf{s}},\hat{\mathbf{s}}')$ is the scattering phase function, which is a normalized density function giving the probability that photons traveling in a range of directions $\hat{\mathbf{s}}\pm\Delta\hat{\mathbf{s}}$ get scattered to the range of direction $\hat{\mathbf{s}}'\pm\Delta\hat{\mathbf{s}}'$.

1. Approximating the phase function

To solve Eq. (A1) we assume functional forms for the phase function and the radiance that converts the BTE into a system of linear partial differential equations that can be analytically solved. We begin by substituting our approximation for the scattering phase function. We choose the δ-Eddington phase function, which takes the form

$$p_{\delta-E}(\hat{\mathbf{s}},\hat{\mathbf{s}}')=\frac{1}{4\pi}\{[(1-f)(1+3g^*)(\hat{\mathbf{s}}\cdot\hat{\mathbf{s}}')] + 2f\delta(1-\hat{\mathbf{s}}\cdot\hat{\mathbf{s}}')\}. \tag{A2}$$

In Eq. (A2) f is the fraction of light that is scattered directly forward, while g^* governs the asymmetry of the phase function. Taking the first moment of this equation gives the relation between the scattering anisotropy g and the δ-Eddington parameters, namely,

$$g=f+(1-f)g^*. \tag{A3}$$

The δ-function component within the δ-Eddington approximation effectively reduces the forward scattering that must be accommodated by the $\hat{\mathbf{s}}\cdot\hat{\mathbf{s}}'$ term in the phase function. This allows the diffuse component of the radiance $L_d(\mathbf{r},\hat{\mathbf{s}},t)$ (defined below) to be less anisotropic and improves the radiance approximation close to boundaries. We note that for biological tissues, optical scattering is well described by the Henyey-Greenstein phase function [20]. To best approximate the Henyey-Greenstein phase function we require the second moment of the δ-Eddington phase function to match that of the Henyey-Greenstein phase function. This results in the following expressions for f and g^* [18]:

$$f=g^2,\quad g^*=\frac{g}{g+1}. \tag{A4}$$

To incorporate the δ-Eddington approximation into the BTE, we substitute Eq. (A2) into Eq. (A1) which gives

$$\frac{1}{v}\frac{\partial L(\mathbf{r},\hat{\mathbf{s}},t)}{\partial t}+\hat{\mathbf{s}}\cdot\boldsymbol{\nabla}L(\mathbf{r},\hat{\mathbf{s}},t) = -\mu_t^* L(\mathbf{r},\hat{\mathbf{s}},t)+\mu_s^*\int_{4\pi}L(\mathbf{r},\hat{\mathbf{s}}',t)p_E(\hat{\mathbf{s}},\hat{\mathbf{s}}')d\Omega + S(\mathbf{r},\hat{\mathbf{s}},t). \tag{A5}$$

In Eq. (A5) $\mu_s^*=\mu_s(1-f)$, $\mu_t^*=(\mu_a+\mu_s^*)$, and $p_E(\hat{\mathbf{s}},\hat{\mathbf{s}}')$ is the Eddington phase function given by

$$p_E(\hat{\mathbf{s}},\hat{\mathbf{s}}')=\frac{1}{4\pi}[1+3g(\hat{\mathbf{s}}\cdot\hat{\mathbf{s}}')]. \tag{A6}$$

2. Approximating the radiance

We now implement a functional form for the radiance approximation. We decompose the radiance $L(\mathbf{r},\hat{\mathbf{s}},t)$ into contributions from collimated light $L_c(\mathbf{r},\hat{\mathbf{s}},t)$, which represents unattenuated light from external or internal sources, and diffuse light $L_d(r,\hat{s},t)$, which represents light that has been scattered from these sources. This gives

$$L(\mathbf{r},\hat{\mathbf{s}},t)=L_c(\mathbf{r},\hat{\mathbf{s}},t)+L_d(\mathbf{r},\hat{\mathbf{s}},t). \tag{A7}$$

Substituting Eq. (A7) into Eq. (A5) and dropping the source term gives

$$\frac{1}{v}\frac{\partial}{\partial t}[L_c(\mathbf{r},\hat{\mathbf{s}},t)+L_d(\mathbf{r},\hat{\mathbf{s}},t)]+\hat{\mathbf{s}}\cdot\boldsymbol{\nabla}[L_c(\mathbf{r},\hat{\mathbf{s}},t)+L_d(\mathbf{r},\hat{\mathbf{s}},t)] = -\mu_t^*[L_c(\mathbf{r},\hat{\mathbf{s}},t)+L_d(\mathbf{r},\hat{\mathbf{s}},t)]+\mu_s^*\int_{4\pi}[L_c(\mathbf{r},\hat{\mathbf{s}}',t) + L_d(\mathbf{r},\hat{\mathbf{s}}',t)]p_E(\hat{\mathbf{s}},\hat{\mathbf{s}}')d\Omega. \tag{A8}$$

The collimated contribution to the radiance is given by

$$L_c(\mathbf{r},\hat{\mathbf{s}},t)=\frac{1}{2\pi}P(\mathbf{r},\hat{\mathbf{s}},t)\delta(1-\hat{\mathbf{s}}\cdot\hat{\mathbf{s}}_0), \tag{A9}$$

where $P(\mathbf{r},\hat{\mathbf{s}},t)$ is the irradiance of the collimated source and the factor $\delta(1-\hat{\mathbf{s}}\cdot\hat{\mathbf{s}}_0)/2\pi$ has units sr^{-1}. The factor of $1/2\pi$ is present because the source light is collimated and thus hemispheric. Thus, in the medium the collimated portion of the fluence rate $\varphi_c(\mathbf{r},t)$ is

$$\varphi_c(\mathbf{r},t)=\int_{4\pi}L_c(\mathbf{r},\hat{\mathbf{s}},t)d\Omega=P(\mathbf{r},\hat{\mathbf{s}}_0,t). \tag{A10}$$

Simplifying Eq. (A8) using the relations

$$\hat{\mathbf{s}}\cdot\boldsymbol{\nabla}L_c(\mathbf{r},\hat{\mathbf{s}},t)=-\mu_t^*L_c(\mathbf{r},\hat{\mathbf{s}},t), \tag{A11}$$

$$\int_{4\pi}\mu_s p(\hat{\mathbf{s}},\hat{\mathbf{s}}')L_c(\mathbf{r},\hat{\mathbf{s}}',t)d\Omega=\mu_s^*P(\mathbf{r},\hat{\mathbf{s}}_0,t)p_E(\hat{\mathbf{s}},\hat{\mathbf{s}}_0) \tag{A12}$$

and replacing $L_c(\mathbf{r},\hat{\mathbf{s}},t)$ with Eq. (A9) results in a transport equation for $L_d(\mathbf{r},\hat{\mathbf{s}},t)$ with two terms representing the contribution from a ''primary'' light source as

$$\frac{1}{v}\frac{\partial L_d(\mathbf{r},\hat{\mathbf{s}},t)}{\partial t}+\hat{\mathbf{s}}\cdot\boldsymbol{\nabla}L_d(\mathbf{r},\hat{\mathbf{s}},t)+\mu_t^* L_d(\mathbf{r},\hat{\mathbf{s}},t)$$
$$=\mu_s^*\int_{4\pi}L_d(\mathbf{r},\hat{\mathbf{s}}',t)p_E(\hat{\mathbf{s}},\hat{\mathbf{s}}')d\Omega$$
$$+\mu_s^* P(\mathbf{r},\hat{\mathbf{s}}_0,t)p_E(\hat{\mathbf{s}},\hat{\mathbf{s}}_0)-\frac{1}{2\pi v}\frac{\partial}{\partial t}P(\mathbf{r},\hat{\mathbf{s}},t)\,\delta(1-\hat{\mathbf{s}}\cdot\hat{\mathbf{s}}_0). \tag{A13}$$

Equation (A13) is simply a variant of the BTE with the collimated and diffuse portions of the radiance separated and the δ-Eddington approximation for the phase function specified. We now adopt an approximate functional form for the diffuse radiance. Specifically, we approximate the diffuse radiance by the sum of the first two terms in the series of Legendre polynomials. This is the P_1 approximation and expresses the diffuse radiance as a linear combination of an isotropic term and a term that varies with cos θ. Thus

$$L_d(\mathbf{r},\hat{\mathbf{s}},t)\approx\frac{1}{4\pi}\int_{4\pi}L_d(\mathbf{r},\hat{\mathbf{s}},t)d\Omega$$
$$+\frac{3}{4\pi}\int_{4\pi}L_d(\mathbf{r},\hat{\mathbf{s}}',t)\hat{\mathbf{s}}'\cdot\hat{\mathbf{s}}\;d\Omega' \tag{A14}$$
$$=\frac{1}{4\pi}\,\varphi_d(\mathbf{r},t)+\frac{3}{4\pi}\,\mathbf{j}(\mathbf{r},t)\cdot\hat{\mathbf{s}}, \tag{A15}$$

where $\varphi_d(\mathbf{r},t)$ is the diffuse (i.e., isotropic) component of the fluence rate defined by

$$\varphi_d(\mathbf{r},t)=\int_{4\pi}L_d(\mathbf{r},\hat{s},t)d\Omega \tag{A16}$$

and $\mathbf{j}(\mathbf{r},t)$ is the radiant flux defined by

$$\mathbf{j}(\mathbf{r},t)=\int_{4\pi}L_d(\mathbf{r},\hat{\mathbf{s}}',t)\hat{\mathbf{s}}'\cdot\hat{\mathbf{s}}\;d\Omega'. \tag{A17}$$

3. Governing equations in the P_1 approximation

To get the first of the governing equations in the diffusion approximation, an energy balance is performed by substituting Eq. (A15) into Eq. (A13) and integrating over all 4π steradians. This gives

$$\frac{1}{v}\frac{\partial\varphi_d(\mathbf{r},t)}{\partial t}+\boldsymbol{\nabla}\cdot\mathbf{j}(\mathbf{r},t)+\mu_a\varphi_d(\mathbf{r},t)$$
$$=\mu_s^* P(\mathbf{r},\hat{\mathbf{s}}_0,t)-\frac{1}{v}\frac{\partial P(\mathbf{r},\hat{\mathbf{s}}_0,t)}{\partial t}. \tag{A18}$$

The second equation is generated by performing a flux balance. This is done by substituting Eq. (A15) into Eq. (A13), multiplying each term in the resulting equation by $\hat{\mathbf{s}}$, and integrating over all 4π steradians. This gives

$$\frac{1}{v}\frac{\partial\mathbf{j}(\mathbf{r},t)}{\partial t}+\mu_{\mathrm{tr}}\,\mathbf{j}(\mathbf{r},t)$$
$$=-\frac{1}{3}\,\boldsymbol{\nabla}\varphi_d(\mathbf{r},t)+g^*\mu_s^* P(\mathbf{r},\hat{\mathbf{s}}_0,t)\hat{\mathbf{s}}_0$$
$$-\frac{1}{v}\frac{\partial}{\partial t}[\hat{\mathbf{s}}_0 P(\mathbf{r},\hat{\mathbf{s}}_0,t)]. \tag{A19}$$

We wish to eliminate $\mathbf{j}(\mathbf{r},t)$ to get an equation that relates the diffuse fluence rate $\varphi_d(\mathbf{r},t)$ with the collimated fluence rate or irradiance $P(\mathbf{r},\hat{\mathbf{s}}_0,t)$. Solving Eq. (A19) for $\mathbf{j}(\mathbf{r},t)$ gives an expression that is identical to Eq. (2). Substituting Eq. (2) into Eq. (A18) and simplifying gives the P_1 approximation to the radiative transport equation using the δ-Eddington phase function approximation and is identical to Eq. (1).

APPENDIX B: DC SOLUTION FOR A SEMI-INFINITE SPHERE

In this appendix we present the method of solution for the dc diffuse fluence rate in a semi-infinite spherical geometry as represented by Eq. (9) and subject to boundary conditions given by Eqs. (11) and (13). Equation (9) is an inhomogeneous Helmholtz equation that we solve by convolving the inhomogeneous (or source) term with the Green's function for this equation [21] and satisfies the boundary conditions with appropriate surface integrals. Following the approach taken by Prahl [22], we start with Green's second identity, which states [23]

$$\int\;(u\nabla^2 v-v\nabla^2 u)d\mathcal{V}'=\int\left(u\,\frac{\partial v}{\partial n}-v\,\frac{\partial u}{\partial n}\right)d\mathcal{S}', \tag{B1}$$

where n is the direction defined by the outward normal to the surface S', which encloses the volume $\mathcal{V}'$ containing the sources. Setting $u=G^{\mathrm{dc}}(\mathbf{r}|\mathbf{r}')$ and $v=\varphi_d^{\mathrm{dc}}(\mathbf{r}')$, we have

$$\int\;[G^{\mathrm{dc}}(\mathbf{r}|\mathbf{r}')\nabla^2\varphi_d^{\mathrm{dc}}(\mathbf{r}')-\varphi_d^{\mathrm{dc}}(\mathbf{r}')\nabla^2 G^{\mathrm{dc}}(\mathbf{r}|\mathbf{r}')]d\mathcal{V}'$$
$$=\int\left[G^{\mathrm{dc}}(\mathbf{r}|\mathbf{r}')\,\frac{\partial\varphi_d^{\mathrm{dc}}(\mathbf{r}')}{\partial n}-\varphi_d^{\mathrm{dc}}(\mathbf{r}')\,\frac{\partial G^{\mathrm{dc}}(\mathbf{r}|\mathbf{r}')}{\partial n}\right]d\mathcal{S}', \tag{B2}$$

where $G^{\mathrm{dc}}(\mathbf{r}|\mathbf{r}')$ is understood to be the solution to the equation

$$\nabla^2 G^{\mathrm{dc}}(\mathbf{r}|\mathbf{r}')-3\mu_a\mu_{\mathrm{tr}}G^{\mathrm{dc}}(\mathbf{r}|\mathbf{r}')=-\delta(\mathbf{r}-\mathbf{r}'), \tag{B3}$$

with *homogeneous* boundary conditions, that is, $G^{\mathrm{dc}}(\mathbf{r}|\mathbf{r}')-Ah\boldsymbol{\nabla}G^{\mathrm{dc}}(\mathbf{r}|\mathbf{r}')\cdot\hat{\mathbf{r}}=0$ at $r=r_0$ and $G^{\mathrm{dc}}(\mathbf{r}|\mathbf{r}')\to 0$ as $r\to\infty$.

To simplify the left-hand side of Eq. (B2), we first subtract $\int G^{\mathrm{dc}}(\mathbf{r}|\mathbf{r}')3\mu_a\mu_{\mathrm{tr}}\varphi_d^{\mathrm{dc}}(\mathbf{r}')d\mathcal{V}'$ and reduce using Eq. (9). We then add back this same term and simplify using Eq. (B3). This gives

$$\int [G^{\mathrm{dc}}(\mathbf{r}|\mathbf{r}')\nabla^2\varphi_d^{\mathrm{dc}}(\mathbf{r}') - \varphi_d^{\mathrm{dc}}(\mathbf{r}')\nabla^2 G^{\mathrm{dc}}(\mathbf{r}|\mathbf{r}')]d\mathcal{V}'$$
$$= \varphi_d^{\mathrm{dc}}(\mathbf{r}) - 3\mu_s^*(\mu_t + g^*\mu_a)\int G^{\mathrm{dc}}(\mathbf{r}|\mathbf{r}')P^{\mathrm{dc}}(\mathbf{r}')d\mathcal{V}'. \tag{B4}$$

We expand the right-hand side of Eq. (B2) by noting that at $r=r_0$, $\partial/\partial n = -\partial/\partial r$, while at $r\to\infty$, $\partial/\partial n = \partial/\partial r$; thus

$$\int \left[G^{\mathrm{dc}}(\mathbf{r}|\mathbf{r}')\frac{\partial\varphi_d^{\mathrm{dc}}(\mathbf{r}')}{\partial n} - \varphi_d^{\mathrm{dc}}(\mathbf{r}')\frac{\partial G^{\mathrm{dc}}(\mathbf{r}|\mathbf{r}')}{\partial n}\right]d\mathcal{S}'$$
$$= -\int_{r=r_0}\left[G^{\mathrm{dc}}(\mathbf{r}|\mathbf{r}')\frac{\partial\varphi_d^{\mathrm{dc}}(\mathbf{r})}{\partial r} - \varphi_d^{\mathrm{dc}}(\mathbf{r})\frac{\partial G^{\mathrm{dc}}(\mathbf{r}|\mathbf{r}')}{\partial r}\right]d\mathcal{S}'$$
$$+\int_{r\to\infty}\left[G^{\mathrm{dc}}(\mathbf{r}|\mathbf{r}')\frac{\partial\varphi_d^{\mathrm{dc}}(\mathbf{r})}{\partial r} - \varphi_d^{\mathrm{dc}}(\mathbf{r})\frac{\partial G^{\mathrm{dc}}(\mathbf{r}|\mathbf{r}')}{\partial r}\right]d\mathcal{S}'. \tag{B5}$$

Substituting the inhomogeneous boundary condition specified by Eq. (11) into Eq. (B5), equating the result with Eq. (B4) and solving for $\varphi_d^{\mathrm{dc}}(\mathbf{r})$ gives

$$\varphi_d^{\mathrm{dc}}(\mathbf{r}) = 3\mu_s^*(\mu_t^* + g^*\mu_a)\int G^{\mathrm{dc}}(\mathbf{r}|\mathbf{r}')P^{\mathrm{dc}}(\mathbf{r}')d\mathcal{V}'$$
$$-3g^*\mu_s^*\left[\int_{r'=r_0} P^{\mathrm{dc}}(\mathbf{r}')G^{\mathrm{dc}}(\mathbf{r}|\mathbf{r}')d\mathcal{S}'\right.$$
$$\left.-\int_{r'\to\infty} P^{\mathrm{dc}}(\mathbf{r}')G^{\mathrm{dc}}(\mathbf{r}|\mathbf{r}')d\mathcal{S}'\right], \tag{B6}$$

where $P^{\mathrm{dc}}(\mathbf{r}) = P_0\exp[-\mu_t^*(r-r_0)]/4\pi r^2$.

Using Eq. (B6), we can now solve for $\varphi_d^{\mathrm{dc}}(\mathbf{r})$. The Green's function for Eq. (9) is [21]

$$G^{\mathrm{dc}}(\mathbf{r}|\mathbf{r}') = \frac{1}{4\pi|\mathbf{r}-\mathbf{r}'|}\exp(-\mu_{\mathrm{eff}}|\mathbf{r}-\mathbf{r}'|). \tag{B7}$$

Direct substitution of Eqs. (7) and (B7) into Eq. (B6) gives the solution to Eq. (9) as

$$\varphi_d^{\mathrm{dc}}(\mathbf{r}) = 3\mu_s^*(\mu_t^* + g^*\mu_a)\int_{\mathcal{V}}\frac{1}{4\pi|\mathbf{r}-\mathbf{r}'|}$$
$$\times\exp(-\mu_{\mathrm{eff}}|\mathbf{r}-\mathbf{r}'|)\frac{P_0\exp[-\mu_t^*(r'-r_0)]}{4\pi r'^2}d^3\mathbf{r}'$$
$$-3g^*\mu_s^*\left[\int_{r'=r_0}\frac{1}{4\pi|\mathbf{r}-\mathbf{r}'|}\exp(-\mu_{\mathrm{eff}}|\mathbf{r}-\mathbf{r}'|)\right.$$
$$\times\frac{P_0\exp[-\mu_t^*(r'-r_0)]}{4\pi r'^2}d^2\mathbf{r}'$$
$$-\int_{r'\to\infty}\frac{1}{4\pi|\mathbf{r}-\mathbf{r}'|}\exp(-\mu_{\mathrm{eff}}|\mathbf{r}-\mathbf{r}'|)$$
$$\left.\times\frac{P_0\exp[-\mu_t^*(r'-r_0)]}{4\pi r'^2}d^2\mathbf{r}'\right]. \tag{B8}$$

Note that the third integral is equal to zero since $\exp[-\mu_t^*(r'-r_0)]\to 0$ as $r'\to\infty$. Since the problem exhibits radial symmetry, we perform the integration using spherical coordinates. Thus $d^3\mathbf{r}' = r'^2dr'\sin\theta'd\theta'd\phi'$ and $d^2\mathbf{r}' = r'^2\sin\theta'd\theta'd\phi'$. The result is identical to that stated by Eq. (14).

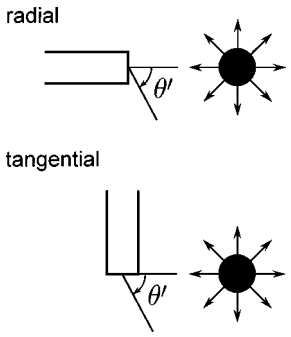

FIG. 10. The coordinate system for the solid angle integrations used to calculate the measured irradiance for radial and tangential fiber orientations.

APPENDIX C: DERIVATION OF THE MEASURED IRRADIANCE FOR RADIAL AND TANGENTIAL DETECTION

Here we derive expressions for the measured irradiances I_r and I_t in terms of the collimated and diffuse fluence rates and the radiant flux. Figure 10 is a schematic of the geometry used for the calculations in radial and tangential fiber orientations. We assume that the light field does not vary significantly across the fiber face. In this case, the measured irradiance for radial orientation $I_r(r,\theta)$ is given by

$$I_r(r,\theta) = \varphi_c^{\mathrm{dc}}(\mathbf{r}) + \int_{\theta'=\pi/2-\theta}^{\pi/2}\int_{\phi'=0}^{2\pi}\left[\frac{\varphi_d^{\mathrm{dc}}(r)}{4\pi}\cos\theta'\right.$$
$$\left.+\frac{3\mathbf{j}^{\mathrm{dc}}(r)}{4\pi}\cos^2\theta'\right]\sin\theta'd\theta'd\phi', \tag{C1}$$

where θ' is the altitude, ϕ' is the azimuthal angle, and $\theta\equiv[\sin^{-1}(N)/n]$, where N is the numerical aperture of the collection fiber, and n is the refractive index of the turbid media.

For tangential detection, there is no contribution from the collimated fluence rate since the orientation of the fiber is not collinear with the photon emission from the source. Further, there is no contribution from the radiant flux since its magnitude varies as $\cos\theta'$ and displays odd symmetry with respect to the fiber axis which is at $\theta'=\pi/2$. Thus only the diffuse fluence rate contributes and the measured irradiance for tangential orientation $I_t(r,\theta)$ is given by

$$I_t(r,\theta) = \int_{\theta'=0}^{\theta}\int_{\phi'=0}^{2\pi}\frac{\varphi_d^{\mathrm{dc}}(r)}{4\pi}\sin\left(\frac{\pi}{2}-\theta'\right)\sin\theta'd\theta'd\phi'. \tag{C2}$$

Integration of Eqs. (C1) and (C2) results in Eqs. (27) and (28),

[1] R. A. DeBlasi, S. Fantini, M. A. Franceschini, M. Ferrari, and E. Gratton, Med. Biol. Eng. Comput. **33**, 228 (1995).
[2] H. Jiang, K. D. Paulsen, U. L. Osterberg, B. W. Pogue, and M. S. Patterson, J. Opt. Soc. Am. A **13**, 253 (1996).
[3] R. Manoharan, Y. Wang, and M. S. Feld, Spectrochim. Acta A **52**, 215 (1996).
[4] B. J. Tromberg *et al.*, Philos. Trans. R. Soc. London, Ser. B **352**, 661 (1997).
[5] J. Wu, M. S. Feld, and R. P. Rava, Appl. Opt. **32**, 3585 (1993).
[6] R. Richards-Kortum and E. M. Sevick-Muraca, Annu. Rev. Phys. Chem. **47**, 555 (1996).
[7] D. J. Durian and J. Rudnick, J. Opt. Soc. Am. A **14**, 235 (1997).
[8] J. B. Fishkin, S. Fantini, M. J. vandeVen, and E. Gratton, Phys. Rev. E **53**, 2307 (1996).
[9] S. T. Flock, M. S. Patterson, B. C. Wilson, and D. R. Wyman, IEEE Trans. Biomed. Eng. **36**, 1162 (1989).
[10] R. C. Haskell *et al.*, J. Opt. Soc. Am. A **11**, 2727 (1994).
[11] S. A. Prahl, Ph.D. thesis, University of Texas at Austin, 1988 (unpublished).
[12] W. M. Star, in *Dosimetry of Laser Radiation in Medicine and Biology*, edited by G. J. Müller and D. H. Sliney (SPIE, Bellingham, WA, 1989), pp. 146–154.
[13] W. M. Star, in *Optical-Thermal Response of Laser-Irradiated Tissue*, edited by A. J. Welch and M. J. C. van Gemert (Plenum, New York, 1995), pp. 131–206.
[14] A. Ishimaru, *Wave Propagation and Scattering in Random Media* (Academic, New York, 1978), Vol. 2.
[15] H. J. van Staveren, C. J. M. Moes, J. van Marle, S. A. Prahl, and M. J. C. van Gemert, Appl. Opt. **30**, 4507 (1991).
[16] G. M. Hale and M. R. Querry, Appl. Opt. **12**, 555 (1973).
[17] S. Fantini, M. A. Franceschini, and E. Gratton, J. Opt. Soc. Am. B **11**, 2128 (1994).
[18] J. H. Joseph, W. J. Wiscombe, and J. A. Weinman, J. Atmos. Sci. **33**, 2452 (1976).
[19] S. Fantini, M. A. Franceschini, and E. Gratton, Appl. Opt. **36**, 156 (1997).
[20] S. L. Jacques, C. A. Alter, and S. A. Prahl, Lasers Life Sci. **1**, 309 (1987).
[21] A. Ishimaru, *Wave Propagation and Scattering in Random Media* (Ref. [14]), Vol. 1.
[22] S. A. Prahl, in *Optical Thermal Response of Laser-Irradiated Tissue* (Ref. [13]), pp. 207–231.
[23] G. F. Roach, *Green's Functions* (Cambridge University Press, Cambridge, 1982).